





Localized standing waves induced by spatiotemporal forcing

P. J. Aguilera-Rojas ¹, M. G. Clerc ¹, G. Gonzalez-Cortes ¹ and G. Jara-Schulz ^{1,2}

¹*Departamento de Física and Millennium Institute for Research in Optics, Facultad de Ciencias Físicas y Matemáticas, Universidad de Chile, Casilla 487-3, Santiago, Chile*

²*Centre de Nanosciences et de Nanotechnologies, CNRS, Université Paris-Saclay, Palaiseau 91120, France*



(Received 6 March 2021; accepted 14 September 2021; published 19 October 2021)

Particle-type solutions are observed in out-of-equilibrium systems. These states can be motionless, oscillatory, or propagative depending on the injection and dissipation of energy. We investigate a family of localized standing waves based on a liquid-crystal light valve with spatiotemporal modulated optical feedback. These states are nonlinear waves in which energy concentrates in a localized and oscillatory manner. The organization of the family of solutions is characterized as a function of the applied voltage. Close to the reorientation transition, an amplitude equation allows us to elucidate the origin of these localized states and establish their bifurcation diagram. Theoretical findings are in qualitative agreement with experimental observations. Our results open the possibility of manipulating localized states induced by light, which can be used to expand and improve the storage and manipulation of information.

DOI: [10.1103/PhysRevE.104.044209](https://doi.org/10.1103/PhysRevE.104.044209)

I. INTRODUCTION

One of the most attractive phenomena of macroscopic systems is that when locally perturbed, they can exhibit corpuscular or particlelike solutions [1–4]. Namely, localized dynamical behaviors are observed, characterized by a continuous parameter, its position, and discrete parameters that account for mobility, charge, and width, among other features. The most paradigmatic and pioneering example is the observation of solitary waves when disturbing a water channel—*solitons* [5–7]. During the last decade, a great effort has been put into the extension of this soliton concept from conservative systems to dissipative ones—*dissipative localized structures* [1–4]. These scientific efforts have a twofold purpose: on the one hand, fundamental to understand the nature, dynamics, interaction, and mechanisms of creation and annihilation of these intriguing particlelike behaviors, and on the other hand, to generate possible applications in particular in the field of optical storage and transmissions [1–4,8]. The possibility that light can induce localized states, which can be manipulated, stored, and retrieved, is fundamental for future optical applications. Dissipative structures have been observed in different fields, such as domains in magnetic materials, chiral bubbles in liquid crystals, current filaments in gas discharge, spots in chemical reactions and optical systems, localized states in driven fluid surface waves, oscillons in granular media, isolated states in thermal convection, solitary waves in nonlinear optics, among others (see reviews [1–4], and references therein). From a theoretical point of view, to one-dimensional systems, localized states can be described, geometrically speaking, as spatial trajectories that connect a steady state with itself. Namely, they are homoclinic orbits on the phase portrait associated to the stationary system (see [9], and references therein). In two dimensions there is no general geometric description of these localized structures,

except in the case that the solutions have axial symmetry [10]. In general, these two-dimensional solutions are commonly understood as a balance of the interface energy and the different energy between the connected states [9].

The prerequisite to observe localized structures is the coexistence of states. Depending on the type of states, localized structures evidence different features [9]. In the case of uniform states, the localized structures usually have tails with damped spatial oscillations. These solutions appear and disappear by saddle-node bifurcations [1,4]. Various localized states of different sizes can also coexist. These solutions as a function of the parameters present an intricate bifurcation diagram, denominating *collapsed snaking* [11,12]. This scenario changes dramatically when a uniform and pattern state coexist, giving rise to the *localized patterns* [13,14]. These solutions are characterized by exhibiting a pattern surrounded by a homogeneous state. A family of localized patterns can coexist as a function of the physical parameters and present a complex organization called the homoclinic snaking bifurcation diagram [15]. The localized patterns and their bifurcation diagram are a consequence of the interaction of fronts between the states that constitute them [16]. Note that similar behavior and characteristics exhibit the localized structures built up by two patterns [17]. Experimentally, considering a liquid-crystal layer with a photosensitive wall and a spatially modulated optical feedback, localized patterns and their respective snaking bifurcation diagrams were observed [18]. Note that spatial forcing induces uniform states to become patterns, and therefore pinning between these patterns is responsible for the emergence of these localized patterns [1–4,19]. Oscillatory localized solutions in conservative systems—*breathers* or *oscillons*—have also drawn community attention [6,7]. The extension of these solutions in parametrically forced systems has been theoretically predicted [20–22]. The experimental

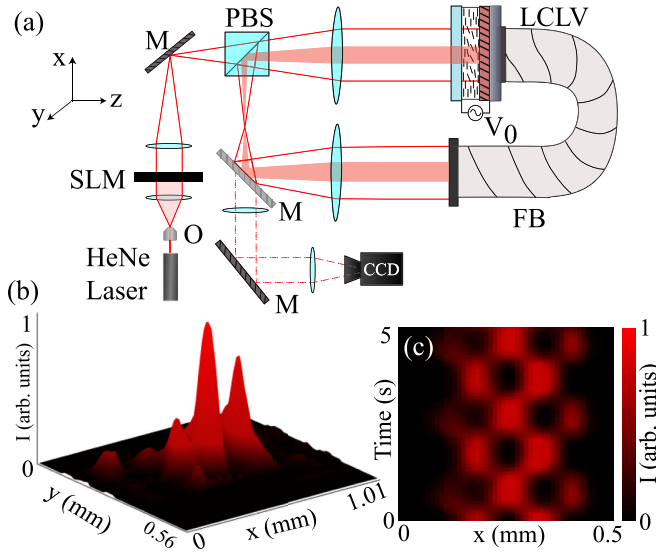


FIG. 1. Experimental localized standing wave state. (a) Schematic representation of a liquid-crystal light valve (LCLV) with optical spatiotemporal modulated feedback. SLM accounts for the spatial light modulator, M are mirrors, PSB is the polarized beam splitter, and V_0 is the driven voltage applied to LCLV. O is an optical objective, and FB is a fiber bundle. (b) shows an experimental 3D-spatial view of a localized standing wave and (c) shows a spatiotemporal evolution for the same structure. The color scale shows the intensity of the detected light. This standing wave was obtained at $V_0 = 2.800V_{rms}$.

observation and mechanism that originates standing waves in dissipative media are not established since a standing waves coexistence with another state and pinning phenomenon is required. These standing waves correspond to localized oscillatory patterns. Figure 1 illustrates an oscillatory pattern experimentally observed. However, due to the oscillation, the pinning effect or nucleation barrier is not expected.

This article aims to experimentally and theoretically investigate localized standing waves. Based on a liquid-crystal light valve with spatiotemporal modulated optical feedback, we observe a family of localized standing waves and the coexistence between them. Their bifurcation diagram as a function of the driven voltage is revealed. Theoretically, based on an amplitude equation valid close to reorientation molecular instability, localized waves are observed, and the organization of the family of these localized oscillatory patterns is established. The amplitude equation allows us to settle the origin of the blocking mechanism of domains between standing waves. Theoretical and experimental findings show a qualitative agreement.

II. EXPERIMENTAL SETUP

A liquid-crystal light valve (LCLV) in an optically modulated feedback loop allows us to observe localized standing waves (see Fig. 1). The LCLV is a flexible device that exhibits bistability, pattern formation, and localized structures when placed in an optical feedback [24]. The LCLV consists of a nematic liquid crystal LC-654 (NIOPIK) with dielec-

tric anisotropy $\epsilon_a = 10.7$ placed between two glass layers separated by a distance $d = 15 \mu\text{m}$. Transparent indium tin oxide electrodes and a photoconductive layer are deposited on the glasses to subject the liquid crystal to a driven voltage. A dielectric Bragg mirror with optimized reflectivity for 632.8 nm light is placed in the back layer of the liquid-crystal cell. The LCLV can be electrically addressed by applying an oscillatory voltage V_0 rms and frequency $f = 1.0$ kHz across the liquid-crystal layer. Furthermore, the system is optically forced with a He-Ne laser ($\lambda_0 = 632$ nm). The LCLV is placed in a $4f$ optical configuration ($f = 25$ cm), as indicated in Fig. 1(a). The optical feedback circuit is closed with an optical fiber bundle (FB) placed at a distance $4f$ from the LCLV front face. The optical fiber bundle injects the light into the photoconductive layer, applying an additional voltage to the liquid-crystal material depending on the light intensity. The light entering the optical loop is spatiotemporally tailored with a transmissive spatial light modulator (SLM) and the polarizing beam splitter (PBS). Thus, the intensity profile of the illumination before reaching the LCLV has the form

$$I = \begin{cases} I_0 + I_1 \cos(\omega t) \cos\left(\frac{2\pi x}{\lambda}\right), & |x| \leq x_0 \text{ and } |y| \leq y_0 \\ 0, & |x| > x_0 \text{ and } |y| > y_0, \end{cases}$$

where $I(x, y, t)$ is the light intensity at a point (x, y) at instant t in the LCLV layer front face, I_0 a constant background light intensity, I_1 the modulated light amplitude intensity, ω the oscillation frequency of the light, and λ the wavelength of the illumination. x_0 and y_0 are parameters that characterize the illuminated channel ($y_0 < x_0$). All experiments were conducted with $\omega = 0.5$ rad/s and $\lambda = 0.16 \pm 0.01$ mm. The light injected into the LCLV is polarized in the y direction. The LCLV boundary planar anchoring is 45° to the y axis. When the voltage applied to the LCLV is above a threshold voltage V_T the liquid-crystal molecules undergo a reorientational transition following the electric field applied—the Fréedericksz transition [23]. The molecular reorientation changes the birefringence of the material, inducing a relative change in the phase and polarization of the light reflected in the dielectric mirror, which induces a modulation in the intensity coupling the liquid-crystal orientation with the voltage exerted to the liquid-crystal layer [24]. A small portion of intensity is extracted from the optical loop to perform the measurements and monitor the system. The light intensity is recorded with a CMOS camera. The different average molecular orientation can be detected as different intensities in the light profile. All experimental observations are conducted at room temperature (20° C).

III. EXPERIMENTAL LOCALIZED STANDING WAVES

When optical feedback is homogeneous ($I_1 = 0$), we can characterize the bistability cycle between the planar and reoriented state [25–27]. Black asterisks and circles account for homogeneous states in the bifurcation diagram shown in Fig. 2(a). The lower and upper branches account for the planar and reoriented states, respectively. When considering the spatiotemporal forcing ($I_1 \neq 0$), the planar and reoriented states become standing waves. The bifurcation diagram between the standing waves shifts to the left with respect to the coexistence region between homogeneous states [see the red asterisks and

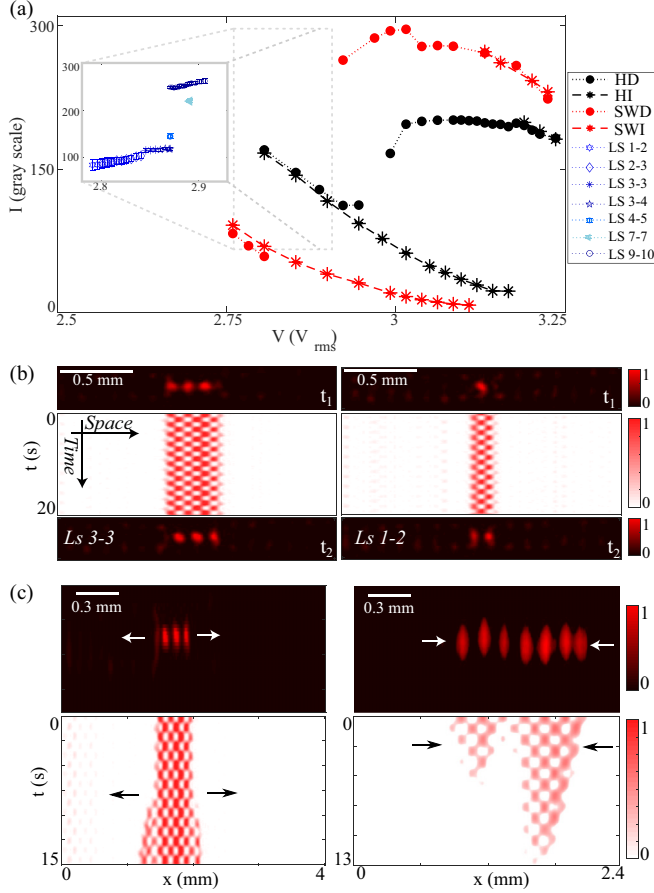


FIG. 2. (a) Bifurcation diagram of localized waves. Average light intensity over a cycle I as a function of the driven voltage V_0 . H and SW account for uniform states and homogeneous standing waves (at $I_1 = 0.056$ mW), by increasing (I) or decreasing (D) the voltage in the experiment. LS n - m accounts for the localized standing wave with n and m bump in an oscillation cycle. (b) Spatiotemporal evolution, initial (t_1) and final (t_2) states for different localized standing waves. Left and right panels account for localized standing wave 3-3 and 1-2, respectively. (c) Experimental expansion, $V_0 = 2.878V_{\text{rms}}$ (left), and contraction, $V_0 = 2.700V_{\text{rms}}$ (right), of the localized structure. The top and bottom panels are instantaneous profiles and spatiotemporal diagrams, respectively. The arrows indicate the propagation of the upper standing wave.

circles in Fig. 2(a)]. Hence, the system exhibits a bistability between the standing waves and then one would expect to find localized standing waves between these states. Employing the spatial light modulator, we can control the initial condition and induce localized waves. Figure 1 shows a localized standing wave and its respective spatiotemporal evolution. By changing the initial condition, thanks to the spatial light modulator, we observe a family of localized oscillatory patterns with different widths. Figure 2(b) shows different localized standing waves and their respective spatiotemporal diagrams. Note that there are solutions that connect an even (odd) number with another one of the oscillations after one cycle [cf. left panels of Fig. 2(b)] and also there are solutions with even and odd oscillations after one cycle [see the right panels of Fig. 2(b)]. Monitoring the total intensity, we have character-

ized the bifurcation diagram of the localized standing waves. Figure 2(a) summarizes the diagram found. This diagram is characterized by exhibiting a snakelike bifurcation diagram [15]. A similar bifurcation diagram was observed for localized patterns in a LCLV with spatial modulated optical feedback [18]. When the driven voltage V_0 decreases (increases) and crosses a critical value, the localized standing waves disappear as these localized solutions begin to contract (expand) [see Fig. 2(c)].

IV. THEORETICAL DESCRIPTION OF LCLV WITH SPATIOTEMPORAL OPTICAL FEEDBACK

The liquid-crystal light valve experiment is shown schematically in Fig. 1(a). The polarized light of intensity I_{in} is generated by a He-Ne laser and expanded by a Kepler telescope for later tailoring by the spatial light modulator, producing a spatiotemporal modulated light with the profile $I_{\text{in}}(x, t) = I_0 + I_1 \cos(\omega t) \cos(2\pi x/\lambda)$, where x accounts for the transverse coordinate in the direction that LCLV is illuminated, I_0 a constant background light intensity, I_1 the modulated light amplitude intensity, ω the oscillation frequency of the light, and λ the wavelength of the illumination. Subsequently, the ray of light crosses the polarizer beam splitter to meet the liquid-crystal light valve, crossing it and reflected by the dielectric mirror. As a result of this process, the light acquires a phase shift $\phi = \beta \cos \theta$ that depends on the average tilt of the molecules of the liquid crystal $\theta(x)$ [28], $\beta \equiv 2dk_0\Delta n$, where d is the liquid-crystal cell thickness, $k_0 = 2\pi/\lambda_0$ is the optical wave number, λ_0 is the wavelength of the beam, and Δn is the refractive index difference between the ordinary and extraordinary axis. Subsequently, the light beam is re-injected into the back of the LCLV, which contains a photoconductor. Namely, the feedback loop is closed by an optical fiber bundle and is designed to avoid the diffraction effect, and polarization interference is present [24,28,29]. The light intensity I_w reaching the photoconductor is given by [24,29]

$$\begin{aligned} I_w(\theta) &= \frac{I_{\text{in}}(x, t)}{2} |1 + e^{-i\beta \cos^2 \theta}|^2 \\ &= I_{\text{in}}(x, t) \{1 + \cos(\beta \cos^2 \theta)\}. \end{aligned} \quad (1)$$

As long as I_{in} is sufficiently small ($I_{\text{in}} \sim \text{mW/cm}^2$), the effective voltage, V_{eff} , applied to the liquid-crystal layer can be expressed as $V_{\text{eff}} = \Gamma V_0 + \alpha I_w(\theta)$, $0 < \Gamma < 1$ is a transfer factor that depends on the electrical impedances of the photoconductor, dielectric mirror, and liquid crystal, while α is a phenomenological dimensional parameter that describes the linear response of the photoconductor [24]. In our experiment $\Gamma = 0.3$ and $\alpha = 5.5 \text{ V cm}^2/\text{mW}$. Therefore, the dynamics exhibited by the LCLV with optical feedback, is that the liquid-crystal molecular orientation changes the phase of light emerging from the LCLV which, due to the optical feedback, induces a voltage that reorients the liquid-crystal molecules. Thanks to the optical circuit, the liquid-crystal molecular orientation self-induces a nonlinear spatiotemporal dynamics.

Our liquid-crystal light valve constitutes a nematic liquid crystal. These soft materials are high viscosity fluids. Hence, the dynamics of the average director tilt $\theta(x, t)$ is described

by a nonlocal relaxation equation of the form [24,29,30]

$$\tau \partial_t \theta = l^2 \partial_{xx} \theta - \theta + \begin{cases} 0, & V_0 \leq V_{\text{FT}}, \\ \frac{\pi}{2} \left(1 - \sqrt{\frac{\Gamma V_{\text{FT}}}{\Gamma V_0 + \alpha I_w(\theta, x, t)}} \right), & V_0 > V_{\text{FT}}, \end{cases} \quad (2)$$

with $V_{\text{FT}} \approx 3.2V_{\text{rms}}$ the threshold for the Fréedericksz transition, $\tau = 30$ ms is the liquid-crystal relaxation time, and $l = 30 \mu\text{m}$ the electric coherence length. From here on, we will consider that $V_0 > V_{\text{FT}}$, in the case of considering the system without spatiotemporal forcing ($I_1 = 0$). The average director tilt equilibrium θ_0 for voltages lower than that of the Fréedericksz transition is null ($\theta_0 = 0$), and for higher values it is

$$\theta_0 = \frac{\pi}{2} \left(1 - \sqrt{\frac{\Gamma V_{\text{FT}}}{\Gamma V_0 + \alpha I_w(\theta)}} \right), \quad (3)$$

where $\{V_0, I_0\}$ are the experimental control parameters. In other words, these are the parameters that are modified to characterize the dynamics of the system. To figure out the dynamics of model Eq. (2), we study its dynamics around the emergence of bistability, i.e., when the system becomes multivalued or exhibits a nascent of bistability [31]. When the function $\theta_0(V_0, I_0)$ has a saddle point at $V_0 = V_c$ and $I_0 = I_c$, this function becomes multivalued. Around the saddle point $\theta_0(V_c, I_c) = \theta_c$ creates two new extreme points that determine the size of the bistability region. To find the saddle points, we have to impose the conditions

$$\left. \frac{d\theta_0}{dV_0} \right|_{\{V_c, I_c\}} = 0, \quad \left. \frac{d^2\theta_0}{d^2V_0} \right|_{\{V_c, I_c\}} = 0, \quad (4)$$

and, after straightforward algebraic calculations, we obtain the relations [30]

$$I_c = \frac{\pi^2 V_{\text{FT}}}{\alpha \beta (\pi/2 - \theta_c)^3 \sin(2\theta_c) \sin(\beta \cos^2 \theta_c)},$$

$$3 = (\theta_c - \pi/2)[2 \csc 2\theta_c + \beta \sin 2\theta_c \cot(\beta \cos^2 \theta_c)]. \quad (5)$$

The first expression gives the critical value of I_0 for which θ_0 becomes multivalued. The second expression is an algebraic equation that depends only on the parameter β and determines all the points of the nascent of bistability. Notice that only half of them have physical significance because the other half corresponds to negative values of the intensity. By taking into account the constraint that the intensity must be positive and considering that the cotangent function is π periodic, we have that the actual number of points of the nascent of bistability is equal to the next smallest integer of $\beta/2\pi$. β is about 54, for the values considered in our experiment; then one expects to find eight points of the nascent of bistability in the entire (V_0, I_0) parameter space, a prediction that is confirmed by the experiment [24].

Close to the nascent of bistability point ($I_0 \equiv I_c$ and $V_0 \equiv V_c$) and considering the ansatz

$$\theta(x, t) \approx \theta_c + \Theta(x, t)/\Theta_0, \quad (6)$$

where $\Theta_0^2 \equiv 2\beta \cos 2\theta_c \cot(\beta \cos^2 \theta_c) + (4 + \beta^2 \sin 2\theta_c)/3 - 2/(\pi/2 - \theta_c)^2$, into Eq. (2) and developing in Taylor series by keeping the cubic terms, assuming spatial forcing as a

perturbative effect ($I_1 \ll 1$), after straightforward algebraic calculations, we obtain

$$\partial_T \Theta = \eta + \mu \Theta - \Theta^3 + \partial_{XX} \Theta + \gamma \sin(\omega t) \cos(\kappa x), \quad (7)$$

where

$$\eta \equiv \frac{\alpha \delta (\pi/2 - \theta_c)^3}{\pi^2 V_{\text{FT}}} \left[I_0 - I_c + \alpha \delta \frac{V_0 - V_c}{2} \right], \quad (8)$$

$$\mu \equiv \frac{12\Gamma}{\pi^2 V_{\text{FT}}} \left[(\pi/2 - \theta_c)^2 (V_0 - V_c) + \left(\frac{\pi^2 V_{\text{FT}}}{12} - (\pi/2 - \theta_c)^2 \right) \frac{I_0 - I_c}{I_c} \right], \quad (9)$$

$$\gamma \equiv \frac{\alpha \delta (\pi/2 - \theta_c)^3}{\pi^2 V_{\text{FT}}} I_1, \quad (10)$$

$$T \equiv \frac{t}{\tau}, \quad (11)$$

$$X \equiv \frac{x}{l}, \quad (12)$$

$$\delta \equiv [1 - \cos(\beta \cos^2 \theta_c)], \quad (13)$$

$$\kappa \equiv \frac{2\pi}{\lambda}. \quad (14)$$

Therefore, close to the nascent of bistability, model Eq. (2) can be approximated by a simple bistable model Eq. (7), which describes the dynamics observed around this critical point. η and μ are bifurcation parameters [32], η controls the bistability region, and μ accounts for the transition between equilibria. The third and fourth terms on the right-hand side of Eq. (7) account for nonlinear elasticity and diffusive coupling, respectively. The last term accounts for the spatiotemporal forcing, where $\kappa = 2\pi/\lambda$.

V. THEORETICAL LOCALIZED STANDING WAVES

The homogeneous solutions of the unforced model Eq. (7) describe the nascent of bistability (cusp catastrophe) [32]. Namely, the system has a region of the parameter space η - μ , where it exhibits bistability. Nevertheless, in this region, no stable localized structures are observed. This scenario changes radically when one considers the spatiotemporal forcing ($\gamma \neq 0$). Figure 3 shows the typical localized standing waves numerically observed and their respective bifurcation diagram. The conducted numerical study considers simulations of model Eq. (7) with Neumann boundary conditions. Integration was implemented using a fourth-order explicit Runge-Kutta scheme with a fixed time-step size and a finite difference scheme in space with a centered stencil of three grid points.

To shed light on the origin of the observed localized states, let us consider the high-frequency limit $\omega \rightarrow \infty$ [33], where analytical calculations are most accessible. Considering the following ansatz $\Theta(x, t) = u(x, t) - \gamma \cos(kx) \cos(\omega t)/\omega$ in Eq. (7), $\kappa = k$, and taking into account the dominant terms, one gets

$$\partial_t u = \eta + \tilde{\mu} u - u^3 + \partial_{xx} u + \frac{\gamma(k^2 - \mu)}{\omega} \cos(kx) \cos(\omega t) - \frac{3\gamma^2}{4\omega^2} \cos(2kx) u, \quad (15)$$

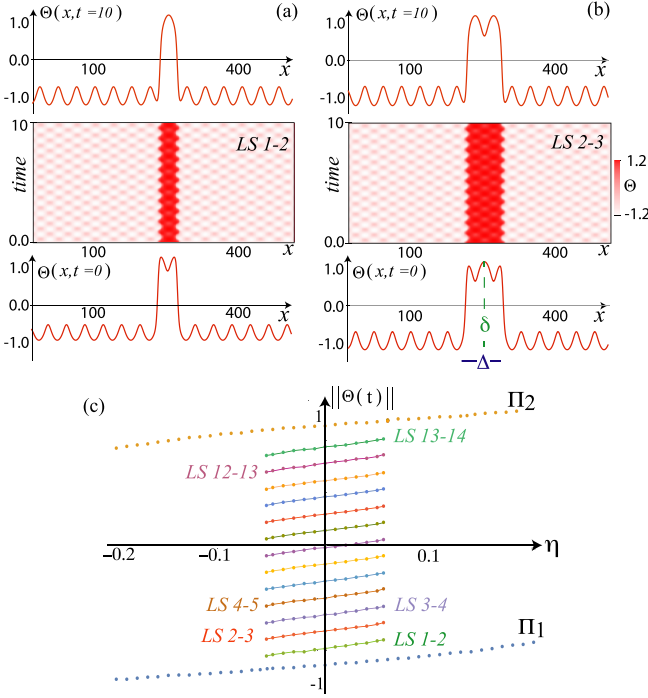


FIG. 3. Localized standing waves obtained by numerical simulations of the bistable model Eq. (7) with $\mu = 1.0$, $\lambda = 0.035$, $\omega = 0.53$, and $\gamma = 0.5$. (a) and (b) Localized standing wave profiles and spatiotemporal diagram between 1-2 and 2-3 bumps in an oscillation cycle. The middle panels account for the spatiotemporal evolution of the localized standing waves. δ and Δ account for the position and width of localized standing waves. (c) Bifurcation diagram of model Eq. (7) with $\mu = 1.0$, $\lambda = 0.07$, $\omega = 4$, and $\gamma = 2$. Total area $\|\Theta(t)\| = \int \Theta(x, t) dx/L$ as a function of the bifurcation parameter η . L is the system size. Π_1 and Π_2 account for the upper and lower standing extended waves, respectively. LS n - m accounts for the localized standing wave with n and m bump in an oscillation cycle.

where $u(x, t)$ accounts for the average temporal evolution of Θ over the ω frequency and $\tilde{\mu} \equiv \mu - 3\gamma^2/4\omega^2$. The last two terms on the right-hand side stand for the dominant corrections. As a result of the rapid oscillations, the bifurcation parameter $\tilde{\mu}$ is renormalized, explaining the shift of the experimental bifurcation diagram to the left with respect to the coexistence region between homogeneous states (see Fig. 2). The first and last corrections account for spatiotemporal and space forcing, respectively. This last term is responsible for a nucleation barrier and the pinning phenomenon between the two equilibria. Systems with this type of spatial forcing are well known to exhibit localized structures [16–18,34]. With the unperturbed system ($\gamma = 0$) near the Maxwell point, the system exhibits domain walls of the form $u_F(x - x_0) = \sqrt{\tilde{\mu}} \tanh[\sqrt{\tilde{\mu}}(x - x_0)/2]$. Localized standing waves can be built up as the interaction of two successive domains of the form [16]

$$u = u_F\left(x - \delta(t) + \frac{\Delta(t)}{2}\right) - u_F\left(x - \delta(t) - \frac{\Delta(t)}{2}\right) - \sqrt{\tilde{\mu}} + w, \quad (16)$$

where $\delta(t)$ and $\Delta(t)$ account for the centroid and width of the localized standing wave (cf. Fig. 3), and $w(\delta, \Delta, t)$ is a small correction function. Introducing the previous ansatz in Eq. (15), linearizing in w , and applying a solvability condition after straightforward calculations, we obtain the equations for the position and width of the localized standing wave:

$$\begin{aligned} \dot{\delta} &= b \cos(2k\delta) \sin(k\Delta) - c \sin\left(\frac{k\Delta}{2}\right) \sin(k\delta) \cos(\omega t), \\ \dot{\Delta} &= -a^2 e^{-\sqrt{\mu/2}\Delta} + \tilde{\eta} + b \sin(2k\delta) \cos(k\Delta) \\ &\quad + c \cos\left(\frac{k\Delta}{2}\right) \cos(k\delta) \cos(\omega t). \end{aligned} \quad (17)$$

The full and lengthy expressions of the coefficients $\{a, b, c, \tilde{\eta}\}$, as a function of the LCLV parameters, will be reported elsewhere. Notice that b and c are, respectively, proportional to $(\gamma/\omega)^2$ and γ/ω . The first equation accounts for the dynamics of the position of the localized solution induced by spatiotemporal forcing. As a result of the forcing, the system exhibits positions where the localized structure is fixed [$\delta_n = 2\pi n/k$, $n = 1, 2, \dots$; see right panel Fig. 2(b)] and oscillatory [$\delta_n = \pi(2n - 1)/2k$, $n = 1, 2, \dots$; see left panel Fig. 2(b)]. Equilibrium position disturbances are characterized by oscillations damped toward equilibrium. The second equation accounts for the family of localized standing waves. The first, second, third, and fourth terms, respectively, account for the interaction of the domains, the difference in energy of the equilibria, the nucleation barrier induced by the forcing, and its temporal modulation. The first three terms account for the bifurcation diagram with a snakinglike bifurcation diagram [15]. Figure 3(c) shows the numerical bifurcation diagram of the localized standing wave. The last term accounts for the width oscillations, which are observed in the experiment (see Fig. 2) and numerical simulations (cf. Fig. 3). The snakinglike bifurcation diagram in the numerical analysis is completely vertical [15]; however, experimentally, it is usually tilted due to imperfections and neglected variables [18,34,35]. When voltage or η is decreased (increased), the localized standing waves disappear by a saddle-node mechanism that causes the localized solutions to begin to contract (expand) [see Figs. 2(c) and 4 for experimental and numerical results, respectively].

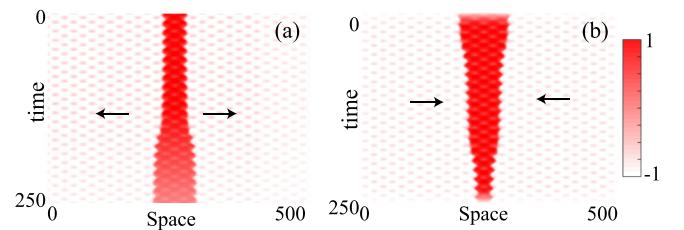


FIG. 4. Destabilization of localized standing waves. Numerical expansion, $\eta = -0.04$ (a), and contraction, $\eta = 0.04$ (b), of the localized standing wave of model Eq. (1) by $\mu = 1.0$, $\lambda = 0.035$, $\omega = 0.53$, and $\gamma = 0.5$.

VI. CONCLUSIONS

We have shown the existence, dynamical evolution, and bifurcation diagram of localized standing waves in a liquid-crystal light valve with spatiotemporal modulated optical feedback in which a light beam induces a family of localized standing waves. Our results show the possibility of manipulating localized states induced by light, which can be used to extend and enhance previously developed schemes for information storage and retrieval as elementary pixels [36] as well as all-optical image processing [37]. Likewise, the different states found can allow the efficient use of multiple

information channels. The use of spatiotemporal forcing can provide a systematic way of inducing localized structures in optical bistable systems [38], such as semiconductor and fiber cavities.

ACKNOWLEDGMENTS

This work was funded by ANID–Millennium Science Initiative Program–ICN17_012. M.G.C. is thankful for financial support from the Fondecyt 1210353 project. G.G.-C. acknowledges the support of ANID-CONICYT-PFCHA Doctorado Nacional 2017211716.

-
- [1] *Localized States in Physics: Solitons and Patterns*, edited by O. Descalzi, M. Clerc, S. Residori, and G. Assanto (Springer, New York, 2010).
- [2] H. G. Purwins, H. U. Bödeker, and Sh. Amiranashvili, Dissipative solitons, *Adv. Phys.* **59**, 485 (2010).
- [3] *Dissipative Solitons: From Optics to Biology and Medicine*, Lecture Notes in Physics Vol. 751, edited by N. Akhmediev and A. Ankiewicz (Springer, Heidelberg, 2008).
- [4] E. Knobloch, Spatial localization in dissipative systems, *Annu. Rev. Condens. Matter Phys.* **6**, 325 (2015).
- [5] J. Scott Russell, *Report on Waves*, Report of the 14th meeting of the British Association for the Advancement of Science, Plates XLVII-LVII (York, 1844), pp. 311–390.
- [6] A. C. Newell, *Solitons in Mathematics and Physics* (Society for Industrial and Applied Mathematics, Philadelphia, 1985).
- [7] M. Remoissenet, *Waves Called Solitons: Concepts and Experiments* (Springer Science & Business Media, Heidelberg, 2013).
- [8] S. Barland *et al.*, Cavity solitons as pixels in semiconductor microcavities, *Nature* **419**, 699 (2002).
- [9] P. Couillet, Localized patterns and fronts in nonequilibrium systems, *Int. J. Bifurcation Chaos* **12**, 2445 (2002).
- [10] D. J. Lloyd and B. Sandstede, Localized radial solutions of the Swift-Hohenberg equation, *Nonlinearity* **22**, 485 (2009).
- [11] P. Couillet, C. Elphick, and D. Repaux, Nature of Spatial Chaos, *Phys. Rev. Lett.* **58**, 431 (1987).
- [12] Y. P. Ma, J. Burke, and E. Knobloch, Defect-mediated snaking: A new growth mechanism for localized structure, *Phys. D (Amsterdam, Neth.)* **239**, 1867 (2010).
- [13] P. Couillet, C. Riera, and C. Tresser, Stable Static Localized Structures in One Dimension, *Phys. Rev. Lett.* **84**, 3069 (2000).
- [14] M. G. Clerc, D. Escaff, and V. M. Kenkre, Patterns and localized structures in population dynamics, *Phys. Rev. E* **72**, 056217 (2005).
- [15] P. D. Woods and A. R. Champneys, Heteroclinic tangles and homoclinic snaking in the unfolding of a degenerate reversible Hamiltonian-Hopf bifurcation, *Phys. D (Amsterdam, Neth.)* **129**, 147 (1999).
- [16] M. G. Clerc and C. Falcon, Localized patterns and hole solutions in one-dimensional extended systems, *Phys. A (Amsterdam, Neth.)* **356**, 48 (2005).
- [17] U. Bortolozzo, M. G. Clerc, C. Falcon, S. Residori, and R. Rojas, Localized States in Bistable Pattern-Forming Systems, *Phys. Rev. Lett.* **96**, 214501 (2006).
- [18] F. Haudin, R. G. Rojas, U. Bortolozzo, S. Residori, and M. G. Clerc, Homoclinic Snaking of Localized Patterns in a Spatially Forced System, *Phys. Rev. Lett.* **107**, 264101 (2011).
- [19] Y. Pomeau, Front motion, metastability and subcritical bifurcations in hydrodynamics, *Phys. D (Amsterdam, Neth.)* **23**, 3 (1986).
- [20] M. G. Clerc, S. Coulibaly, and D. Laroze, Localized waves in a parametrically driven magnetic nanowire, *Europhys. Lett.* **97**, 3000 (2012).
- [21] D. Urzagasti, M. G. Clerc, D. Laroze, and H. Pleiner, Breather soliton solutions in a parametrically driven magnetic wire, *Europhys. Lett.* **104**, 40001 (2013).
- [22] M. G. Clerc, C. Fernandez-Oto, and S. Coulibaly, Pinning-depinning transition of fronts between standing waves, *Phys. Rev. E* **87**, 012901 (2013).
- [23] V. Fréedericksz and V. Zolina, Forces causing the orientation of an anisotropic liquid, *Trans. Faraday Soc.* **29**, 919 (1927).
- [24] S. Residori, Patterns, fronts and structures in a liquid-crystal-light-valve with optical feedback, *Phys. Rep.* **416**, 201 (2005).
- [25] K. Alfaro-Bittner, C. Castillo-Pinto, M. G. Clerc, G. González-Cortés, G. Jara-Schulz, and R. G. Rojas, Front propagation steered by a high-wavenumber modulation: Theory and experiments, *Chaos* **30**, 053138 (2020).
- [26] A. J. Alvarez-Socorro, C. Castillo-Pinto, M. G. Clerc, G. Gonzales-Cortes, and M. Wilson, Front propagation transition induced by diffraction in a liquid crystal light valve, *Opt. Express* **27**, 12391 (2019).
- [27] K. Alfaro-Bittner, C. Castillo-Pinto, M. G. Clerc, G. González-Cortés, R. G. Rojas, and M. Wilson, Front propagation into an unstable state in a forced medium: Experiments and theory, *Phys. Rev. E* **98**, 050201(R) (2018).
- [28] R. Neubecker, G.-L., Oppo, B. Thuerling, and T. Tschudi, Pattern formation in a liquid-crystal light valve with feedback, including polarization, saturation, and internal threshold effects, *Phys. Rev. A* **52**, 791 (1995).
- [29] M. G. Clerc, A. Petrossian, and S. Residori, Bouncing localized structures in a liquid-crystal light-valve experiment, *Phys. Rev. E* **71**, 015205(R) (2005).
- [30] F. Haudin, R. G. Elias, R. G. Rojas, U. Bortolozzo, M. G. Clerc, and S. Residori, Front dynamics and pinning-depinning phenomenon in spatially periodic media, *Phys. Rev. E* **81**, 056203 (2010).

- [31] M. Tlidi, P. Mandel, and R. Lefever, Localized Structures and Llocalized Patterns in Optical Bistability, *Phys. Rev. Lett.* **73**, 640 (1994).
- [32] S. H. Strogatz, *Nonlinear Dynamics and Chaos* (CRC Press, Boca Raton, FL, 2015).
- [33] N. N. Bogoliubov and Y. A. Mitropolski, *Asymptotic Methods in the Theory of Non-Linear Oscillations* (Gordon and Breach, New York, 1961).
- [34] U. Bortolozzo, M. G. Clerc, and S. Residori, Local theory of the slanted homoclinic snaking bifurcation diagram, *Phys. Rev. E* **78**, 036214 (2008).
- [35] W. J. Firth, L. Columbo, and A. J. Scroggie, Proposed Resolution of Theory-Experiment Discrepancy in Homoclinic Snaking, *Phys. Rev. Lett.* **99**, 104503 (2007).
- [36] M. Ichii and P. Davis, Dynamic memory arrays and chaos in a spatial-light-modulator ring circuit, *Opt. Rev.* **3**, A426 (1996).
- [37] G. Häusler and E. Lange, Feedback network with space invariant coupling, *Appl. Opt.* **29**, 4798 (1990).
- [38] H. M. Gibbs, *Optical Bistability: Controlling Light with Light* (Academic, London, 1985).